Local chemical disorder as the origin of anomalous thermal expansion in TiFe2 Laves phase alloys

Azavedo, M.; Dias, E. T.; Srihari, V.; Dankelman, Robert; Dhiman, I.; Priolkar, K. R.

DOI
10.1039/d5cp03136b

Publication date
2025

Document Version
Final published version

Published in
Physical chemistry chemical physics : PCCP

PCCP

ROYAL SOCIETY OF CHEMISTRY

PAPER

View Article Online
View Journal | View Issue

Cite this: *Phys. Chem. Chem. Phys.*, 2025, **27**, 24467

Local chemical disorder as the origin of anomalous thermal expansion in $TiFe_2$ Laves phase alloys

M. Azavedo,[a] E. T. Dias,[a] V. Srihari,[b] Robert Dankelman,[c] I. Dhiman[c] and K. R. Priolkar *[ad]

Received 15th August 2025,
Accepted 20th October 2025

DOI: 10.1039/d5cp03136b

rsc.li/pccp

$TiFe_2$ alloys, a C14 Laves phase system, exhibit negative or zero thermal expansion (NTE/ZTE) despite the absence of the first-order transitions that typically drive such behavior in related compounds. Across the compositional range, the magnetic ground state evolves from ferromagnetic ordering in Fe-rich alloys to antiferromagnetic ordering in Ti-rich variants, yet the thermal expansion response remains invariant. High-resolution synchrotron X-ray and neutron diffraction detect no anomalies in lattice volume or magnetic moment, and Rietveld refinements exclude significant antisite disorder. In contrast, Fe and Ti K-edge extended X-ray absorption fine structure (EXAFS) and elemental mapping *via* energy-dispersive X-ray spectroscopy (EDAX) reveal pronounced nanoscale compositional inhomogeneity, forming Fe-rich and Ti-rich regions. The coexistence of competing ferro- and antiferromagnetic interactions from these chemically distinct domains gives rise to an invar-like effect below a characteristic temperature, T^*. These results establish local chemical disorder as a key mechanism for stabilizing NTE/ZTE behavior in intermetallic systems, independent of long-range structural or magnetic transitions.

1 Introduction

Large and tunable negative thermal expansion (NTE) in the C14-type Laves phase intermetallics is associated with a volume-discontinuous itinerant electron transition from the high-temperature antiferromagnetic (AFM) state to a low-temperature ferromagnetic (FM) state.[1–4] Recently, $Hf_{1-x}Ta_xFe_2$ ($x \geq 0.1$) and $Hf_{1-y}Nb_yFe_2$ ($y \geq 0.65$) alloys have attracted considerable attention for exhibiting giant and tunable NTE near room temperature.[5–16]

The parent compound, $HfFe_2$, is ferromagnetic below its Curie temperature ($T_C \sim 600$ K), while $TaFe_2$ and $NbFe_2$ are antiferromagnetic.[15,17] Partial substitution of Ta or Nb for Hf in $HfFe_2$ alters the magnetic ground state from FM to AFM for $x \approx 0.1$.[5,7,18,19] Here, Hf or Ta/Nb occupy the 4f crystallographic sites while the Fe atoms occupy two non-equivalent positions – 2a and 6h.

The AFM state results from antiparallel spin stacking of alternate Fe 6h planes along the [001] direction. The Fe at the 2a site is magnetically frustrated, lying between the two oppositely aligned, ferromagnetic Fe 6h planes and thus carry negligible moment. Upon cooling, Fe atoms at the 2a site acquire magnetic moment, resulting in a transition of the alloy to a ferromagnetic state.[1,20–24] Concomitant with the AFM to FM transition, the hexagonal unit cell volume expands with $\Delta V/V \sim 1.2\%$ leading to negative thermal expansion.[1,25,26] The transition from a low-volume, low-spin AFM state to high-volume, high-spin FM state is attributed to a moment-volume instability, which is the main cause of anomalous thermal expansion behaviour.[27,28] The NTE in $HfFe_2$ is anisotropic, arising primarily from the expansion of the *a*–*b* plane, in contrast to cubic ScF_3, which exhibits an isotropic NTE of about -10 ppm K^{-1} over a wide temperature range (10–1100 K).[29,30]

The magnitude of the thermal expansion can be tailored and even tuned to achieve zero thermal expansion (ZTE) by introducing Fe vacancies or by introducing additional magnetic exchange interactions. These mechanisms create a strong competition between the positive thermal expansion of the AFM phase and the negative thermal expansion associated with the FM phase.[12,17,24,31–33]

A ZTE or invar-like anomaly was first reported by Wassermann *et al.* in the structurally analogous $Ti_{1-x}Fe_{2+x}$ alloys.[34–36] Stoichiometric $TiFe_2$ is an antiferromagnet with a Nèel temperature around room temperature. Similar to $HfFe_2$-based systems, the Fe atoms at the 6h sites carry magnetic moments

[a] *School of Physical and Applied Sciences, Goa University, Taleigao Plateau, Goa, India. E-mail: krp@unigoa.ac.in; Fax: +91 832 245184; Tel: +91 8669609210*
[b] *High Pressure and Synchrotron Radiation Physics Division, Bhabha Atomic Research Centre, Mumbai 400 085, India*
[c] *Delft University of Technology, Mekelweg 15, Delft 2629, JB, The Netherlands*
[d] *UGC-DAE Consortium for Scientific Research, Khandwa Road, Indore, MP, 452001, India*

with parallel spin alignment within the basal plane and antiferromagnetic stacking of these planes along the *c*-axis, while the Fe atoms at 2a sites remain non-magnetic due to geometric frustration.[37,38]

The magnetic ground state of $TiFe_2$ is highly sensitive to stoichiometry, and a small deviation from the stoichiometry upsets the delicate balance between the ferro- and antiferromagnetic interactions, specifically around a critical concentration of Ti $\sim$ 32.5%. Alloys with Ti content above 32.5% exhibit dominant AFM behaviour, while the Fe-rich compositions favour ferromagnetic ordering. Notably, the energy difference between the FM and AFM states is negligibly small, typically below 2 mRy.[20]

A first-order AFM to FM transition in $TiFe_2$ can also be induced by substituting Ti by Sc or Al.[39–42] Just as in the case of (Hf,Ta)Fe_2 and (Hf,Nb)Fe_2, the anomalous thermal expansion in $TiFe_2$ is attributed to the moment-volume instability associated with a transition from a low-spin (LS) antiferromagnetic state to a high-spin (HS) ferromagnetic state.[34–36] However, the neutron diffraction studies on single crystalline $TiFe_2$ did not reveal any discontinuous volume change associated with the AFM to FM transition. Thus the applicability of the moment-volume instability model appears to be limited in explaining the invar-like behaviour in $TiFe_2$.

The present work focusses on $Ti_{33-x}Fe_{67+x}$ alloys, with $x > 0$ (Fe-rich), and $x < 0$ (Ti-rich) achieved by varying the Ti/Fe ratio between 30 : 70 to 35 : 65. The chosen range covers almost the entire region of C14 phase stability[36] as well as the ground state of the alloys from dominant in FM interactions ($Ti_{30}Fe_{70}$) to AFM interactions ($Ti_{35}Fe_{65}$). A comprehensive study of bulk magnetic and thermal expansion properties, crystal structure, magnetic structure, and local structure around Ti and Fe atoms in $Ti_{33-x}Fe_{67+x}$ alloys highlights the role of nanoscale compositional disorder leading to Ti-rich and Fe-rich regions in the invar-like behavior displayed by these alloys.

2 Experimental

Polycrystalline $Ti_{33-x}Fe_{67+x}$ ($x = -3, -1, 0, 1, 2$) was prepared by arc melting high purity ($>$99.99%) Ti and Fe in an inert argon atmosphere. The ingot was flipped 3–4 times and remelted to ensure homogeneity. The weight loss was less than 1%. The obtained ingot was then cut using a low-power diamond saw into smaller pieces, sealed in an evacuated quartz tube and annealed first at 1000 °C for 5 hours and then at 800 °C for 96 hours, followed by furnace cooling. X-ray diffraction (XRD) measurements were performed on a Rigaku Smart Lab X-ray diffractometer with Bragg–Brentano geometry in the 2θ range of 20° to 100° with a step size of 0.02° using Cu K_α radiation. The phase identification was done using the Le Bail method. The stoichiometry and compositional homogeneity were verified by an energy dispersive X-ray spectroscopy (EDAX) system attached to a field emission scanning electron microscope (FE-SEM) (Zeiss Sigma 360). Prior to the analysis, the samples were polished and mounted on conductive carbon tape. The EDAX system was operated at 20 kV with a working distance of 9 mm. Elemental maps were acquired over selected regions with a resolution of 1024 $\times$ 768 pixels and a dwell time of 600 μs per pixel. Resistivity was measured using the conventional four-probe setup in a closed cycle refrigerator in the temperature interval of 30–400 K. A Cryogenic S-700X SQUID magnetometer was employed for magnetization measurements. For the temperature-dependent magnetization measurements ($M(T)$), the sample was cooled in zero applied field from 300 K to 5 K. Magnetization was recorded in an applied field of 100 Oe, in the temperature interval from 5 K to 390 K while warming (ZFC), while subsequently cooling (FCC) and during the next warming (FCW) cycle. Isothermal magnetization ($M(H)$) measurements were performed in the field range of $\pm$5 T (5 quadrants (5Q)) at select temperatures and from 0 to 5 T (one quadrant (1Q)) at 5 K interval in 200 K $\leq T \leq$ 300 K. For each measurement, the sample was cooled from 390 K to the desired temperature in zero field. Low-temperature thermal expansion measurements were performed by measuring the resistance change of a Kyowa strain gauge in the temperature range of 120–380 K. Temperature dependence of lattice parameters was studied by performing Synchrotron XRD at beamline BL-21, RRCAT, Indore. The data was collected at an energy of 12.7 KeV at various temperatures ranging between 100 K and 300 K. The obtained data were then analyzed using the FullProf Suite, and the lattice constants were obtained. Neutron diffraction measurements were recorded at the PEARL neutron diffractometer at Delft University of Technology[43] on one Fe-rich composition $Ti_{32}Fe_{68}$ and one Ti-rich composition $Ti_{35}Fe_{65}$. The data was collected at several temperatures ranging between 4 K and 400 K in a 2θ range from 11° to 158° using thermal neutrons of wavelength equal to 1.667 Å. JANA 2006 software[44] was employed for Rietveld refinement of the neutron diffraction data to obtain the nuclear and magnetic structures. Local structures of Fe and Ti were investigated by X-ray absorption fine structure (XAFS) spectroscopy at various temperatures ranging between 100 K and 300 K on the P65 beamline at the PETRA III synchrotron source, DESY, Hamburg, Germany using a Si(111) double crystal monochromator and two Si mirrors at an angle of incidence of 2 mrad for higher harmonics suppression, a standard configuration for this energy range.[45] Absorbers were made by stacking 20 mm $\times$ 5 mm strips of scotch tape, uniformly coated with very fine sample powder ($\sim$20 microns). The thickness of the absorbers was adjusted to limit the total absorption to $\leq$2.5 beyond the absorption edge. The incident and the transmitted photon beam intensities were measured using ionization chambers filled with the appropriate gases. At least three scans were recorded at every temperature and averaged to reduce the statistical noise. Data analysis was done using the DEMETER suite.[46]

3 Results

3.1 X-ray diffraction

Fig. 1(a) displays room temperature XRD patterns of all the samples. Le Bail refinements performed on the XRD data confirm the hexagonal C14 crystal structure shown in Fig. 1(b)

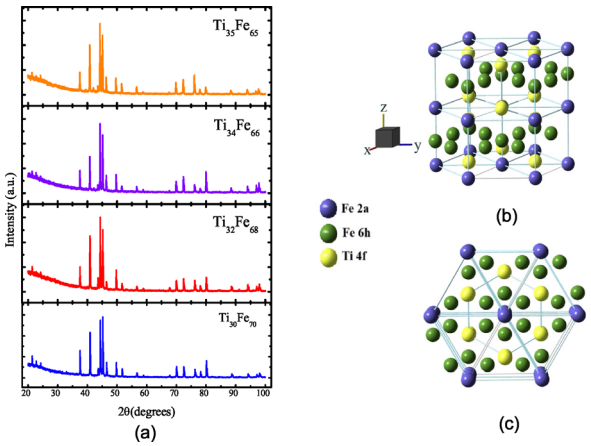

Fig. 1 (a) X-ray diffraction plots for $Ti_{33-x}Fe_{67+x}$ alloys recorded with Cu K_α radiation. (b) Hexagonal unit cell of $TiFe_2$. (c) A top view along the [001] direction of the $TiFe_2$ unit cell.

with space group $P6_3/mmc$. A top view along the [001] direction showing the triangular Fe(6h) networks is displayed in Fig. 1(c). The refined XRD plots are shown in Fig. S1 in the SI. The lattice constants obtained agree well with previous work[38,47] and are listed in Table 1. The increase in the lattice constants with the decrease in the Fe content accords well with the smaller atomic radius of Fe compared to that of Ti. It also confirms the change in the concentration of the alloys. Further confirmation of the alloy compositions was obtained from EDAX. The average compositions determined by scanning several areas of $\sim$200 μm^2 of the sample are listed in Table 1. A maximum of $\sim$3% variation was noted between the EDAX and the nominal compositions of the alloys.

3.2 Thermal expansion

The strain, $\Delta L/L$, calculated from the resistance change of a strain gauge and the thermal expansion coefficient $\alpha = \partial(\Delta L/L)/\partial T$ are plotted in Fig. 2(a) and (b), respectively. The behaviour of α is qualitatively similar to the one reported earlier in the literature.[34] The off-stoichiometric alloys display an invar behaviour from 90 K to around 200 K. At 200 K, α sharply decreases to a maximum value of -2 ppm K^{-1} in $Ti_{32}Fe_{68}$. Post this, α increases until $T > 270$ K and then acquires a small positive value. The crossover from negative to positive values of α varies from 270 K to 315 K depending on the alloy composition.

3.3 Temperature dependent XRD

The temperature dependence of the lattice parameters in the $Ti_{33-x}Fe_{67+x}$ alloys was examined using synchrotron X-ray diffraction in the 2θ range of 12°–52° employing an incident photon energy of 12.7 KeV (λ = 0.9791 Å) over the temperature interval of 100–300 K. As shown in Fig. 3(a), the lattice constant a decreases monotonically with temperature for all compositions. In contrast, the lattice constant c displays a composition dependent trend. For the Fe-rich alloys ($Ti_{30}Fe_{70}$ and $Ti_{32}Fe_{68}$), c decreases with decreasing temperature whereas for Ti-rich alloys ($Ti_{34}Fe_{66}$ and $Ti_{35}Fe_{65}$) c displays a non-monotonic behavior with c initially decreasing and then increasing on cooling (Fig. 3(b)). The unit cell volume of all four alloys plotted in Fig. 3(c) decreases continuously with temperature indicating the absence of any structural transition within the studied temperature range. The c/a ratio shown in Fig. 3(d) exhibits composition-dependent behavior. In the Fe-rich alloys c/a increases slowly and non-monotonically with a steep increase between 250 K and 200 K. In contrast, Ti-rich alloys display a sharp and monotonous increase for all temperatures below 300 K.

Table 1 Lattice parameters, elemental concentrations and EDS compositions of the $Ti_{33-x}Fe_{67+x}$ alloys

Alloy	a Å	c Å	Ti%	Fe%	EDAX composition
$Ti_{30}Fe_{70}$	4.7856	7.8056	28	72	$Ti_{28}Fe_{72}$
$Ti_{32}Fe_{68}$	4.7890	7.8149	30	70	$Ti_{30}Fe_{70}$
$Ti_{34}Fe_{66}$	4.7934	7.8258	34	66	$Ti_{34}Fe_{66}$
$Ti_{35}Fe_{65}$	4.7991	7.8305	37	63	$Ti_{37}Fe_{63}$

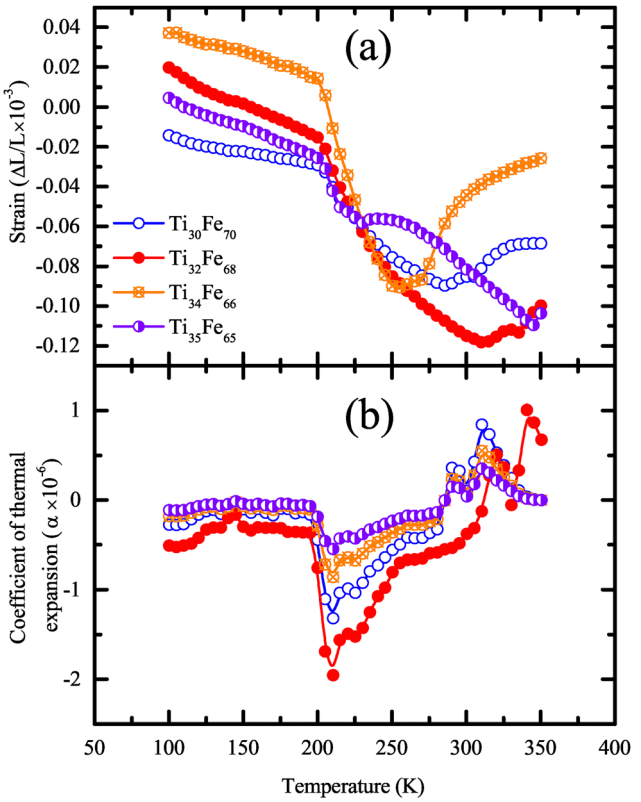

Fig. 2 Variation of (a) thermal expansion and (b) coefficient of linear thermal expansion (α) with temperature in $Ti_{33-x}Fe_{67+x}$ alloys.

3.4 Magnetization measurements

Fig. 4(a)–(d) present the $M(T)$ plots for the $Ti_{33-x}Fe_{67+x}$ alloys recorded in the ZFC, FCC and FCW protocols under an applied field of 0.01 T. Isothermal magnetization curves, $M(H)$, measured in the field interval of $\pm$5 T at selected temperatures in the interval 5 K $\leq T \leq$ 350 K are plotted in Fig. 4(e)–(h). A key trend is the systematic decrease in magnetization with increasing Ti content from $Ti_{30}Fe_{70}$ to $Ti_{35}Fe_{65}$, consistent with earlier reports by Wassermann *et al.*[36] The Fe-rich alloys, $Ti_{30}Fe_{70}$ and

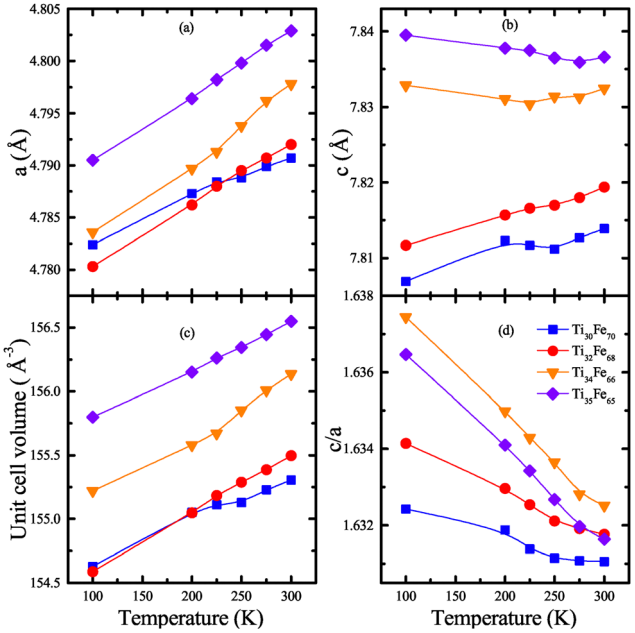

Fig. 3 Thermal evolution of (a) lattice constant *a*, (b) lattice constant *c*, (c) unit cell volume, *V* and (d) *c*/*a* ratio in the $Ti_{33-x}Fe_{67+x}$ alloys.

$Ti_{32}Fe_{68}$ exhibit dominant ferromagnetic behavior. For $Ti_{30}Fe_{70}$, the magnetic ordering temperature T_C exceeds 390 K, as seen in Fig. 4(a), in agreement with the phase diagram reported in ref. 36. Although no saturation of magnetization is observed up to 5 T, the presence of hysteresis in the $M(H)$ loops (Fig. 4(a)) clearly indicates strong ferromagnetic interactions. A distinct kink in the $M(T)$ curve appears at T^* = 220 K. Below this temperature, the $M(H)$ curves exhibit metamagnetic-like transitions that occur at progressively lower fields upon cooling. This behavior may arise from a field-induced spin-state transition of Fe atoms occupying the 2a crystallographic site. Interestingly, near T^*, the thermal expansion coefficient α exhibits a sharp discontinuity, changing from negative to nearly zero (Fig. 2), and remains very low at lower temperatures.

For $Ti_{32}Fe_{68}$ (Fig. 4(b)), a sharp increase in magnetization is observed at around 225 K. However, no corresponding magnetic transition is evident in the derivative of $M(T)$ (Fig. S2 in the SI). Instead, a broad minimum centred around 205 K is seen, indicative of competing magnetic interactions.[7,48] SEM-EDS measurements suggest that the actual composition of this alloy is Fe-rich ($Ti_{30.2}Fe_{69.8}$), which, according to the phase diagram in ref. 36, places it in the ferromagnetic regime with an expected $T_C \approx 375$ K. Although a clear signature is not seen in the $M(T)$ data of this alloy, a deviation from the high-temperature linearity in the M^{-1} *vs.* T plot (Fig. S2 in the SI) appears at about 370 K. Below this temperature, magnetization increases gradually until 220 K followed by a sharp rise resembling a ferromagnetic transition. The $M(H)$ loops in Fig. 4(f) confirm the presence of dominant ferromagnetic interactions at all temperatures below 350 K. Notably, the sharp increase at 220 K again coincides with a discontinuity in α, analogous to that seen in $Ti_{30}Fe_{70}$.

In contrast, the Ti-rich alloys, $Ti_{34}Fe_{66}$ and $Ti_{35}Fe_{65}$ display a markedly different magnetization behavior (see Fig. 4(c) and (d) respectively). Their magnetisation values are more than an order of magnitude smaller than the Fe-rich compositions, with $Ti_{34}Fe_{66}$ exhibiting the lowest overall magnetization. The increase in magnetic moment for $Ti_{35}Fe_{65}$ is likely due to clustering of Fe atoms resulting in the emergence of local ferromagnetic character. This is further supported from the isothermal magnetization plots presented in Fig. 4h as well as the wide separation noticed in the ZFC and FC magnetization curves. Both alloys exhibit two characteristic temperatures, T_1 and T_2, at about 280 K and 220 K, respectively. The high-temperature transition at T_1 is the paramagnetic to antiferromagnetic transition, while the lower-temperature feature at T_2 appears to be similar to that seen in the Fe-rich compositions. The $M(H)$ hysteresis loops plotted in Fig. 4(g) and (h) for $Ti_{34}Fe_{66}$ and $Ti_{35}Fe_{65}$ indicate dominant antiferromagnetic interactions in these alloys.

From the above analysis, it appears that all four $TiFe_2$ alloys – irrespective of their composition – undergo a transition from a low-moment to a high-moment magnetic state at a characteristic temperature $T^* \sim 220$ K and exhibit invar-like behavior below this temperature. To further investigate the nature and significance of T^*, we examine the Arrott plots (M^2 *vs.* H/M), shown in Fig. 5. These plots are constructed within the framework of the mean-field model, using the critical exponent β = 0.5. The value of β characterizes the evolution of the ordered moment below T_C; smaller values of β indicate a more rapid moment growth.[49] Arrott plots also serve as a tool to distinguish the order of magnetic phase transition.[50]

In the present study, a series of isothermal magnetization curves were measured in the temperature interval between 200 K and 300 K with ΔT = 5 K under applied fields varying from 0 to 5 T, to probe the magnetic transition at T^*. Large magnitude, convex shaped Arrott plots, seen for $Ti_{30}Fe_{70}$ signify the presence of strong ferromagnetic interactions. In contrast, $Ti_{34}Fe_{66}$ exhibits highly concave plots with low magnitude, closely resembling a delta function, indicative of dominant antiferromagnetic correlations. Across the series, with increasing Ti content, a progressive evolution from convex to concave Arrott plots (Fig. 5(a)–(d)) reflects the increasing dominance of antiferromagnetic interactions. Notably, no features characteristic of a first-order transition are observed in the vicinity of T^*. For clarity, the curves corresponding to T = 220 K are highlighted in each panel of Fig. 5 and also shown collectively in Fig. 5(e) wherein no discernible signatures of a phase transition are found. However, an interesting field-dependent reversal in magnetization behavior is observed in $Ti_{35}Fe_{65}$. At low fields, $H \leq 1.3$ T, the magnetization decreases with an increase in temperature, while at applied fields $H > 1.3$ T, the trend reverses and magnetization increases with increasing temperature. This metamagnetic behavior is also evident in the M–H isotherms in Fig. 4(h). The anomalies at T^* likely originate from a transition into a state dominated by short-range magnetic order rather than a true long-range ordered phase. This interpretation is supported by the dM/dT plots shown in Fig. S2 (SI), which exhibit no discernible anomalies at T^* for $Ti_{34}Fe_{66}$ and $Ti_{35}Fe_{65}$. Even in $Ti_{32}Fe_{68}$, despite the sharp rise in

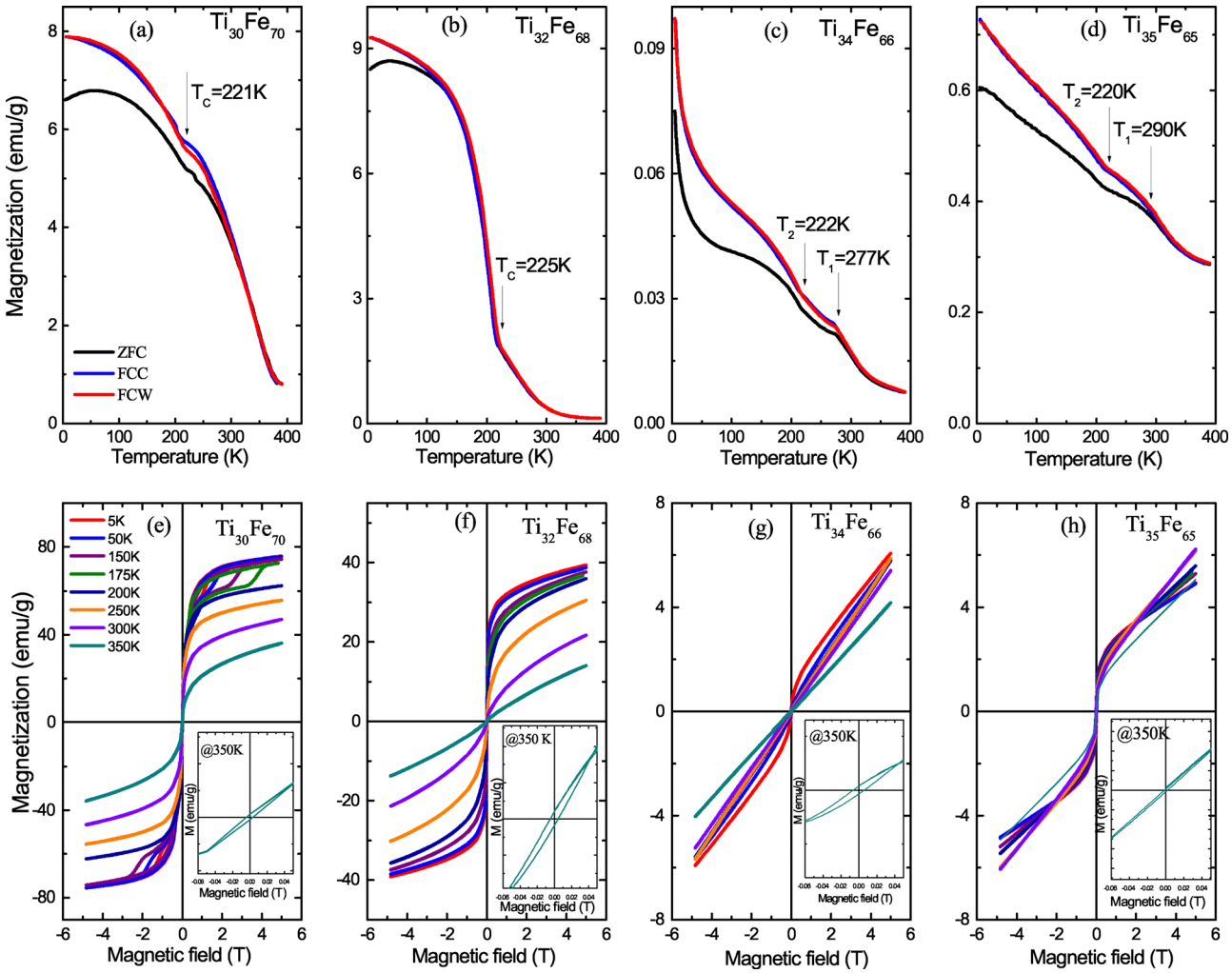

Fig. 4 (a)–(d) Temperature-dependent magnetization, $M(T)$, recorded in the temperature range 5 K $\leq T \leq$ 390 K and (e)–(h) magnetization hysteresis loops recorded at various temperatures in the field range of ±5 T for $Ti_{33-x}Fe_{67+x}$ alloys.

magnetization near T^*, the dM/dT curves show only a broad minimum centred around 200 K. Furthermore, the isothermal $M(H)$ curves show no significant changes across T^*, reinforcing the inference of short-range magnetic interactions.

To complement the above analysis, the magnetic entropy change, ΔS_m was evaluated using the Maxwell's relation, $\Delta S_m(T, 0 \rightarrow H = 5T) = \int_0^H \left(\frac{\partial M}{\partial T}\right)_{H'} dH'$ using the above M–H curves and are plotted in Fig. 6. For $Ti_{30}Fe_{70}$, ΔS_m increases continuously from 200 K to 300 K, reaching a maximum value of -1.4 J kg^{-1} K^{-1} with no peak observed in this temperature range, consistent with an ordering temperature above 300 K. Furthermore, the negative values of ΔS_m confirm a normal magnetocaloric effect, typical of dominant ferromagnetic interactions. ΔS_m is also negative for $Ti_{32}Fe_{68}$ with a broad peak centred around 260 K and a maximum magnitude of $\sim$1.0 J kg^{-1} K^{-1}. Conversely, for the Ti-rich alloys, $Ti_{34}Fe_{66}$ and $Ti_{35}Fe_{65}$, ΔS_m becomes positive below 275 K. A positive entropy change is associated with an inverse magnetocaloric effect and is a hallmark of materials with dominant antiferromagnetic interactions. Importantly, neither Arrott plot analysis nor the temperature dependence of ΔS_m reveals any evidence of a magnetic phase transition occurring at T^*. Resistivity curves measured in the temperature range of 50 K $\leq T \leq$ 400 K also do not show any signature of a phase transition around T^* (see Fig. S3 in the SI).

3.5 Neutron diffraction

Neutron powder diffraction (NPD) measurements were carried out on FM-dominant alloy, $Ti_{32}Fe_{68}$ and AFM-dominant alloy, $Ti_{35}Fe_{65}$ over the temperature range 5–400 K in zero applied magnetic field to elucidate their magnetic structures and assess the possibility of antisite disorder leading to Fe clustering. Prior studies on related systems, such as $HfFe_2$-based alloys, have shown that Fe atoms occupying the 2a site may develop magnetic moments concomitant with the onset of ferromagnetic order, typically attributed to the lifting of geometric frustration due to antisite disorder between Fe and group-IV elements.[24,36,51] Rietveld refinement of the NPD patterns confirms that both alloys retain the C14-type hexagonal Laves

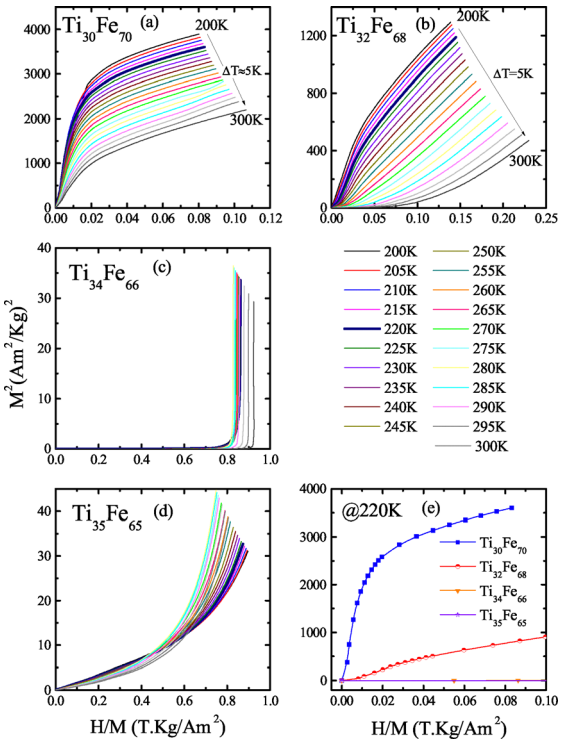

Fig. 5 Arrott plots (M^2 *vs.* H/M) calculated from isothermal magnetization plots recorded every 5 K in the temperature interval 200 K ≤ T ≤ 300 K with field varying from 0 T to 5 T for (a) $Ti_{30}Fe_{70}$, (b) $Ti_{32}Fe_{68}$, (c) $Ti_{34}Fe_{66}$ and (d) $Ti_{35}Fe_{65}$, and (e) Arrott plot at T^* = 220 K for all the samples.

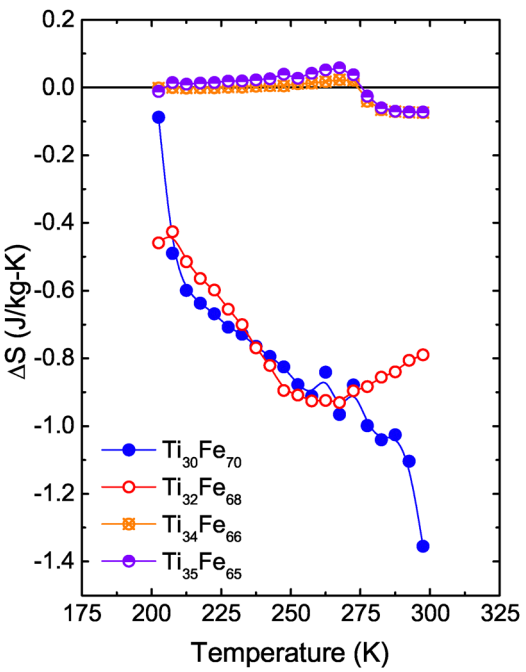

Fig. 6 Magnetic entropy change calculated using the Maxwell relation from the isothermal magnetization data for $Ti_{30}Fe_{70}$, $Ti_{32}Fe_{68}$, $Ti_{34}Fe_{66}$ and $Ti_{35}Fe_{65}$ alloys.

phase structure over the entire temperature range. The refined lattice parameters are in excellent agreement with those obtained from synchrotron X-ray diffraction. The significant contrast in coherent neutron scattering lengths of Ti (b_{Ti} ≈ −3.7 fm) and Fe (b_{Fe} ≈ +9.4 fm) provides sensitivity to potential antisite disorder between Ti and Fe atomic positions. Quantitative analysis reveals approximately 6% antisite disorder in $Ti_{32}Fe_{68}$, wherein Fe atoms partially occupy the 4f sites, and about 4% disorder in $Ti_{35}Fe_{65}$, where Ti atoms occupy a fraction of the 2a sites. These values are consistent with expectations based on stoichiometry. No significant improvement in the fit was achieved by introducing antisite disorder between the 4f and 6h sites, suggesting that such disorder is minimal or absent. The refined structural parameters are tabulated in Tables SI–SIV in the SI.

At 4 K, both alloys exhibit a modest enhancement in the intensity of specific Bragg reflections, indicative of magnetic scattering. The absence of additional magnetic Bragg peaks confirms that the magnetic propagation vector is **k** = (0, 0, 0). Irreducible representational analysis of the Fe atoms at the 6h Wyckoff position was conducted using the BASIREPS module within the FullProf Suite. The Rietveld-refined NPD patterns recorded at 4 K, shown in Fig. 7, are best described by a magnetic structure consisting of Fe(6h) moments antiferromagnetically stacked along the *c*-axis. The refined magnetic

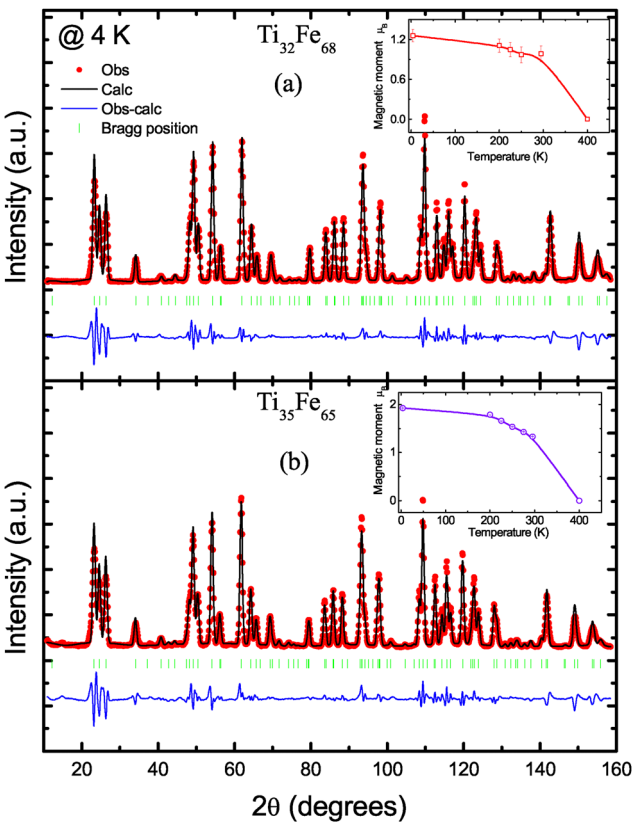

Fig. 7 Rietveld refined Neutron diffraction plots of (a) $Ti_{32}Fe_{68}$ and (b) $Ti_{35}Fe_{65}$ at 4 K. Insets in the respective panels show the thermal evolution of the Fe(6h) magnetic moment in the two alloys.

moment on Fe(6h) is approximately 1.2μ_B for $Ti_{32}Fe_{68}$ and 1.9μ_B for $Ti_{35}Fe_{65}$, in agreement with reported values in the literature. Notably, no magnetic moment could be assigned to Fe at the 2a site in either compositions, contrary to the observed behavior in $HfFe_2$, where the ferromagnetic order coincides with the onset of a finite moment on the 2a sublattice. The absence of moment on Fe at the 2a site could be due to the smaller size of Ti in comparison to Hf, resulting in shorter Fe–Fe and Ti–Fe distances. This increased proximity of Ti and Fe enhances Fe 3d–Ti 3d hybridization and broadens the Fe 3d bands, thereby suppressing the local moment on the Fe(2a) site. The variation of the Fe(6h) moment with temperature in both the alloys is shown as insets in Fig. 7, and no distinct anomaly is observed around T^*.

3.6 Extended X-ray absorption fine structure (EXAFS) spectroscopy study

To investigate the temperature-dependent evolution of the local atomic structure around Ti and Fe, especially in the vicinity of T^*, EXAFS measurements were performed at the Ti and Fe K edges in all the $TiFe_2$ alloy compositions studied here. The EXAFS data collected over a k-range of 3 $Å^{-1}$ to 14 $Å^{-1}$ were Fourier transformed to R-space and analysed in the range for 1 Å to 3 Å in the case of Fe and 1 Å to 4.5 Å for Ti. Fig. S4 in the SI shows the magnitude of the Fourier transforms (FTs) of Ti and Fe EXAFS spectra for all the four alloys measured at 300 K, along with the corresponding fits. The structural model used for fitting was based on the stoichiometric $Ti_{33}Fe_{67}$ alloy wherein Ti atoms occupy the 4f sites and Fe atoms are distributed over the 2a and 6h sites. The local structure around the nonmagnetic Ti atom consists of twelve Fe nearest neighbours: nine Fe atoms at the 6h sites and three Fe atoms at the 2a sites, at an average distance of 2.8 Å, as well as four Ti atoms at ~2.9 Å. These two correlations contribute to the first main peak at ~2.3 Å in the phase uncorrected FT magnitude signals in Fig. S4(a) in the SI. The FT magnitude of Fe EXAFS (Fig. S4(b) in the SI) reflects the local environments of Fe atoms at both 6h and 2a sites. Fe atoms at the 6h position are coordinated by two Fe(6h) neighbors at 2.34 Å (within the same triangle) and an additional two Fe(6h) atoms at 2.45 Å (from adjacent triangles within the plane), along with two Fe(2a) atoms at 2.41 Å and six Ti neighbors at 2.8 Å. Conversely, Fe atoms at the 2a site have six Fe(6h) neighbors at 2.41 Å and six Ti neighbors at 2.8 Å. A comprehensive structural model consisting of all these paths was constructed to fit the Fe and Ti EXAFS together. Apart from the nearest neighbour correlations, two Ti–Fe correlations and one Ti–Ti correlation contributing around 4.5 Å to 4.7 Å were also considered for fitting the Ti EXAFS. Appropriate structural constraints were imposed to reduce the number of fitted parameters. Table SV of the SI lists all varied parameters used in fitting EXAFS data. The fits yielded excellent agreement with the experimental data, and the fitted parameters at individual temperatures for $Ti_{33-x}Fe_{67+x}$ where x = 3, 1, −1 and −2 are respectively compiled in Tables SVI–SIX of the SI.

Fig. 8 presents the temperature dependence of selected interatomic distances: (a) intra-triangle Fe(6h)–Fe(6h), (b) inter-triangle Fe(6h)–Fe(6h), (c) Fe(2a)–Fe(6h), (d) Ti–Fe, and (e) Ti–Ti for the Fe-rich ($Ti_{30}Fe_{70}$ and $Ti_{32}Fe_{68}$) and Ti-rich ($Ti_{34}Fe_{66}$ and $Ti_{35}Fe_{65}$) alloys. As anticipated from the geometry of the C14 structure, the intra- and inter-triangle Fe(6h)–Fe(6h) distances exhibit complementary behavior. While no definitive trends can be discerned within the uncertainty limits near T^* for the majority of bond distances, distinct anomalies are noted in the vicinity of magnetic ordering temperatures in Ti–Ti and Ti–Fe bond distances. This suggests a higher degree of local structural disorder around the Ti atoms across all compositions.

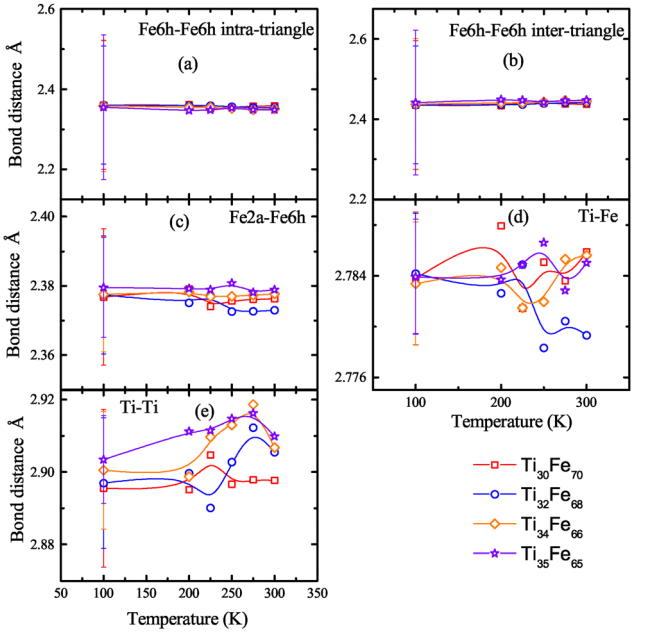

Fig. 8 Variation of (a–c) different Fe–Fe, (d) Ti–Fe and (e) Ti–Ti bond distances obtained from Fe K and Ti K EXAFS analysis in $Ti_{30}Fe_{70}$, $Ti_{32}Fe_{68}$, $Ti_{34}Fe_{66}$, and $Ti_{35}Fe_{65}$ alloys.

To gain deeper insight into the possible origins of the invar-like behaviour in the $TiFe_2$ alloys, we carried out *ab initio* EXAFS simulations using the FEFF8.4 code[52] at the Fe and Ti K edges. Three structural models were considered for these calculations: (i) stoichiometric $TiFe_2$, (ii) a Ti-rich $TiFe_2$ where Ti atoms fully occupying the 2a sites and (iii) a Fe-rich $TiFe_2$ where Fe atoms occupy the 4f sites along with 2a and 6h sites. Simulated EXAFS spectra are compared with the experimental data in both k- and R-space and are shown in Fig. 9.

The measured EXAFS spectra in all four alloys are quite similar to each other and resemble that of stoichiometric $TiFe_2$, indicating that the local structure remains largely similar across the series. However, a detailed comparison reveals key differences. For the Ti K-edge, the experimental EXAFS of all the four alloys exhibit broader features in R-space (Fig. 9(d)) and significantly damped oscillations in k-space (Fig. 9(c)) compared to the calculated spectrum of stoichiometric $TiFe_2$. These deviations signify the presence of pronounced disorder in the local environment of Ti in all the synthesized alloy compositions. Disorder around Fe is also evident from the second group of peaks in the R-range of 3 Å to 5.5 Å in Fig. 9(b). Since Fe's

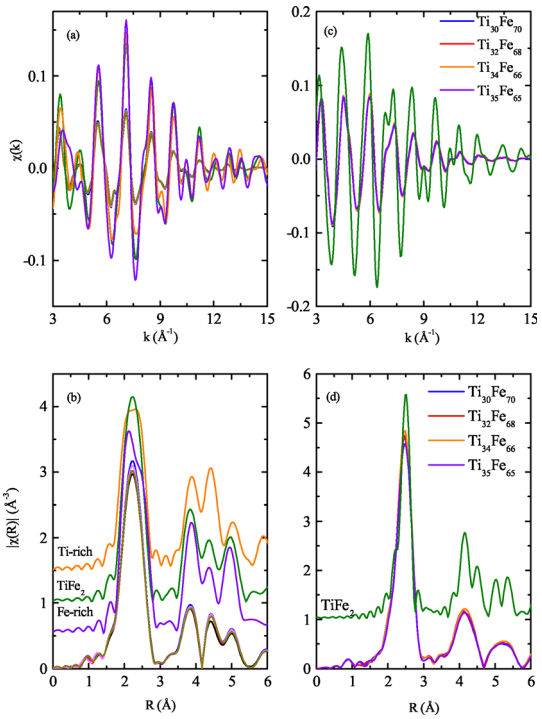

Fig. 9 Comparison of experimental EXAFS signals recorded at the (a) Fe K and (c) Ti K edge and the corresponding FT amplitudes in (b) and (d), respectively, with the FEFF calculated EXAFS signals for stoichiometric, Fe-rich and Ti-rich scenarios. The calculated spectra are vertically shifted for clarity.

nearest neighbours are predominantly Fe atoms, the first FT peak remains relatively unchanged in all four compositions studied here. The local structural disorder is very well corroborated also from the wide thermal variation of Ti–Ti and Ti–Fe bond distances in Fig. 8.

3.7 SEM-EDAX

These structural irregularities are likely driven by antisite disorder involving Ti and Fe atoms, consistent with compositional deviations from ideal stoichiometry. However, the FEFF simulations suggest a degree of local disorder around both Ti and Fe that exceeds what would be expected from antisite mixing alone. To further investigate this, EDAX was performed on polished cross-sections of the alloys. While the average compositions were found to be in good agreement with those listed in Table 1, the spatial mapping revealed the presence of Fe- and Ti-rich clusters of about 300 nm in size dispersed throughout the microstructure. The Ti and Fe stoichiometry, in such clusters, deviated by about 20% from the average composition.

Fig. 10 illustrates this compositional inhomogeneity: Fe-rich alloys show a higher density of Fe-rich clusters (green), while Ti-rich alloys exhibit a predominance of Ti-rich regions (red). Such nanoscale/microscale segregation is consistent with earlier reports on $TiFe_2$-based systems,[51] and appears to be an intrinsic feature of these intermetallic alloys. The presence of these compositionally distinct nanoclusters likely enhances local magnetic heterogeneity, leading to dominant ferromagnetic

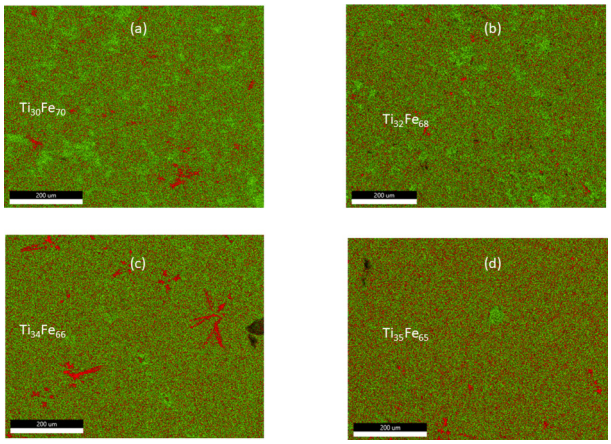

Fig. 10 FESEM-EDS elemental maps recorded over the selected area in (a) $Ti_{30}Fe_{70}$, (b) $Ti_{32}Fe_{68}$, (c) $Ti_{34}Fe_{66}$, and (d) $Ti_{35}Fe_{65}$.

interactions in the Fe-rich alloys and antiferromagnetic interactions in the Ti-rich counterparts. This spatially varying magnetic character provides a plausible microscopic origin for the complex magnetostructural behavior observed across the alloy series, including the anomalous thermal expansion and invar-like effect.

4 Discussion

$TiFe_2$ alloys, which crystallize in the C14-type hexagonal Laves phase structure, exhibit invar-like behavior similar to other isostructural intermetallic compounds. The prevailing mechanisms attribute the invar behaviour to a competition between the moment-volume instability and structural distortions arising due to martensitic transition or high spin–low spin transition.[53,54] In the Laves phase alloys the transition is generally associated with the emergence of a magnetic moment on the Fe atoms occupying the 2a crystallographic site. This feature has been extensively documented in related systems, including (Hf,Ta)Fe_2 and (Hf,Nb)Fe_2 alloys.[7–14] Although $TiFe_2$ is also reported to undergo a low-spin to high-spin transition, no corresponding discontinuity in the unit cell volume is observed.[38] Other distinct differences between $TiFe_2$ and other C14 alloys include the temperature evolution of the lattice parameters. Specifically in (Hf,Ta)Fe_2 and (Hf,Nb)Fe_2, the lattice constant a increases with decreasing temperature while c follows the standard thermal contraction. However, in $TiFe_2$, a and c display opposite temperature dependencies, which is also verified in the present study from Fig. 3.

The temperature dependence of the linear thermal expansion coefficient, $\alpha(T)$, in all the four $TiFe_2$ alloys studied here is qualitatively similar to the earlier reports. Both Fe-rich and Ti-rich compositions exhibit near-zero thermal expansion below a characteristic temperature, $T^* \sim 220$ K. This temperature also coincides with anomalies in the magnetization data, yet signatures of a conventional phase transition at T^* are conspicuously absent in the resistivity measurements, Arrott plots in the 200–300 K temperature interval, and magnetic entropy changes derived from magnetocaloric data. Synchrotron XRD and NPD

measurements also do not show any structural changes around T^*. Furthermore, NPD measurements show only moderate antisite disorder and do not provide evidence for a magnetic moment on Fe(2a) atoms. Similarly, temperature dependence of Fe–Fe, Fe–Ti and Ti–Ti bond distances obtained from EXAFS analysis does not exhibit any clear or consistent trends near T^*. *Ab initio* simulations of Ti and Fe K-edge EXAFS spectra suggest significant structural disorder around both atoms, a conclusion further supported by EDAX-based spatial mapping, which reveals nanoscale segregation into Fe-rich and Ti-rich clusters. Tuning the size and spatial distribution of such clusters, by altering the sample preparation and annealing conditions could be a key for extending the invar behavior over a wider temperature range.

This structural disorder likely gives rise to competing ferromagnetic and antiferromagnetic interactions, particularly evident in the intermediate compositions. As a result, a well-defined magnetic transition is observed only in the two end-member compositions: $Ti_{30}Fe_{70}$ exhibits a ferromagnetic transition above 400 K, while $Ti_{35}Fe_{65}$ displays an antiferromagnetic transition near 277 K. The remaining compositions, $Ti_{32}Fe_{68}$ and $Ti_{34}Fe_{66}$, exhibit strong hysteresis even at 350 K, indicative of competing FM and AFM interactions. In C14 Laves phase alloys, lattice expansion is known to stabilize ferromagnetic ordering through a spin-state transition at the Fe(2a) site, whereas lattice contraction favors antiferromagnetic alignment. The delicate balance between these two types of magnetostructural interactions appears to be the driving force behind the invar-like behavior below T^* in these $TiFe_2$ alloys.

5 Conclusions

The primary objective of this study is to elucidate the underlying mechanism responsible for the negative or zero thermal expansion (NTE/ZTE) behavior observed in $TiFe_2$ alloys. In contrast to other C14 Laves phase systems, which typically exhibit a first-order transition driving anomalous thermal expansion, $TiFe_2$ remains devoid of such a transition, making its thermal response particularly noteworthy. Across the $Ti_{33-x}Fe_{67+x}$ $(-2 \leq x \leq 3)$ compositional range, the magnetic ground state evolves from ferromagnetic ordering in Fe-rich compositions to antiferromagnetic ordering in Ti-rich variants; however, this magnetic crossover does not induce any discernible change in the thermal expansion behavior, which remains effectively composition-invariant. High-resolution synchrotron X-ray diffraction and neutron powder diffraction analyses reveal no detectable anomalies in lattice volume, nor do neutron diffraction measurements indicate any discontinuities in the magnetic moment. Rietveld refinements of the neutron data further confirm the absence of significant antisite disorder within the crystal structure. Instead, the observed NTE/ZTE behavior is attributed to pronounced local compositional inhomogeneities, with Fe-rich and Ti-rich regions evidenced by Fe and Ti K-edge EXAFS analyses and corroborated by elemental mapping using EDAX. The coexistence of competing ferromagnetic and antiferromagnetic interactions, arising from these nanoscale chemical fluctuations, gives rise to the invar-like behavior observed below a characteristic temperature, designated as T^*.

Author contributions

M. Azavedo: data curation, formal analysis, methodology, investigation, validation, visualization and writing – original draft. E. T. Dias: data curation, investigation, resources and writing – review and editing. V. Srihari: data curation, investigation, resources and writing – review and editing. Robert Dankelman: data curation, investigation, resources and writing – review and editing. I. Dhiman: data curation, investigation, resources and writing – review and editing. K. R. Priolkar: conceptualization, data curation, formal analysis, methodology, fund acquisition, resources, validation, visualisation and writing – review and editing.

Conflicts of interest

There are no conflicts to declare.

Data availability

The data supporting this article have been included as part of the supplementary information (SI). The supplementary information contains LeBail refined XRD data, magnetization and resistivity data, Rietveld analysis parameters of the crystal and magnetic structure obtained from neutron diffraction, EXAFS fits to the Fe and Ti K edges and best fit parameters. See DOI: **https://doi.org/10.1039/d5cp03136b**.

Acknowledgements

The authors thank the Council of Scientific and Industrial Research, New Delhi, for financial assistance under 03/1481/2023/EMR-II. We acknowledge DESY (Hamburg, Germany), a member of the Helmholtz Association HGF, for providing experimental facilities. Parts of this research were carried out at Petra III using the P65 beamline. Beamtime was allocated for proposal I-20210145. Support from the Department of Science and Technology, Govt. of India, within the framework of India DESY collaboration is acknowledged. Facilities at the University Laboratory for Materials Characterization, Goa University are also gratefully acknowledged. Neutron powder diffraction data from TU Delft Reactor Institute, Netherlands is deeply appreciated. MA thanks the DST INSPIRE Programme for the fellowship (Grant No. IF 190174).

Notes and references

1 L. Morellon, P. Algarabel, M. Ibarra, Z. Arnold and J. Kamarad, *J. Appl. Phys.*, 1996, **80**, 6911–6914.
2 Z. Ouyang, G. Rao, H. Yang, W. Liu, G. Liu, X. Feng and J. Liang, *J. Alloys Compd.*, 2004, **370**, 18–24.
3 L. Diop, M. Amara and O. Isnard, *J. Phys.: Condens. Matter*, 2013, **25**, 416007.

4 L. Diop, O. Isnard, E. Suard and D. Benea, *Solid State Commun.*, 2016, **229**, 16–21.
5 S. Li, J. Yang, N. Zhao, Q. Wang, X. Fan, X. Yin and W. Cui, *J. Magn. Magn. Mater.*, 2021, **517**, 167236.
6 Y. Nishihara and Y. Yamaguchi, *J. Magn. Magn. Mater.*, 1983, **31**, 77–78.
7 B. Li, X. H. Luo, H. Wang, W. J. Ren, S. Yano, C.-W. Wang, J. S. Gardner, K.-D. Liss, P. Miao, S.-H. Lee, T. Kamiyama, R. Q. Wu, Y. Kawakita and Z. D. Zhang, *Phys. Rev. B*, 2016, **93**, 224405.
8 L. Li, P. Tong, Y. Zou, W. Tong, W. Jiang, Y. Jiang, X. Zhang, J. Lin, M. Wang, C. Yang, X. Zhu, W. Song and Y. Sun, *Acta Mater.*, 2018, **161**, 258–265.
9 L. V. B. Diop, J. Kastil, O. Isnard, Z. Arnold and J. Kamarad, *J. Appl. Phys.*, 2014, **116**, 163907.
10 L. Diop, O. Isnard, M. Amara, F. Gay and J. Itié, *J. Alloys Compd.*, 2020, **845**, 156310.
11 Z. Song, Z. Li, B. Yang, H. Yan, C. Esling, X. Zhao and L. Zuo, *Materials*, 2021, **14**, 5233.
12 J. Xu, Z. Wang, H. Huang, Z. Li, X. Chi, D. Wang, J. Zhang, X. Zheng, J. Shen, W. Zhou, Y. Gao, J. Cai, T. Zhao, S. Wang, Y. Zhang and B. Shen, *Adv. Mater.*, 2023, **35**, 2208635.
13 T. Nakamichi, K. Kai, Y. Aoki, K. Ikeda and M. Yamamoto, *J. Phys. Soc. Jpn.*, 1970, **29**, 794.
14 R. Rawat, P. Chaddah, P. Bag, P. D. Babu and V. Siruguri, *J. Phys.: Condens. Matter*, 2013, **25**, 066011.
15 T. Gao, K. Nishimura, T. Namiki and H. Okimoto, *J. Appl. Phys.*, 2012, **111**, 013913.
16 H. Yibole, A. Pathak, Y. Mudryk, F. Guillou, N. Zarkevich, S. Gupta, V. Balema and V. Pecharsky, *Acta Mater.*, 2018, **154**, 365–374.
17 X. Dong, K. Lin, C. Yu, W. Zhang, W. Li, Q. Zhang, Q. Zhang, J. Liu, Y. Cao and X. Xing, *Scr. Mater.*, 2023, **229**, 115388.
18 P. Bag, R. Rawat, P. Chaddah, P. D. Babu and V. Siruguri, *Phys. Rev. B*, 2016, **93**, 014416.
19 Y. Song, J. Chen, X. Liu, C. Wang, Q. Gao, Q. Li, L. Hu, J. Zhang, S. Zhang and X. Xing, *Chem. Mater.*, 2017, **29**, 7078–7082.
20 H. Wada, N. Shimamura and M. Shiga, *Phys. Rev. B:Condens. Matter Mater. Phys.*, 1993, **48**, 10221.
21 H. Duijn, E. Brück, A. Menovsky, K. Buschow, F. De Boer, R. Coehoorn, M. Winkelmann and K. Siemensmeyer, *J. Appl. Phys.*, 1997, **81**, 4218–4220.
22 Y. Nishihara and Y. Yamaguchi, *J. Phys. Soc. Jpn.*, 1982, **51**, 1333–1334.
23 Y. Song, Q. Sun, M. Xu, J. Zhang, Y. Hao, Y. Qiao, S. Zhang, Q. Huang, X. Xing and J. Chen, *Mater. Horiz.*, 2020, **7**, 275–281.
24 K. Lin, W. Zhang, C. Yu, Q. Sun, Y. Cao, W. Li, S. Jiang, Q. Li, Q. Zhang, K. An, Y. Chen, D. Yu, J. Liu, K. Kato, Q. Zhang, L. Gu, X. Kuang, Y. Tang, J. Miao and X. Xing, *Cell Rep. Phys. Sci.*, 2023, **4**, 101254.
25 Y. Muraoka, M. Shiga and Y. Nakamura, *J. Phys. Soc. Jpn.*, 1976, **40**, 905–906.
26 Y. Nishihara and Y. Yamaguchi, *J. Phys. Soc. Jpn.*, 1983, **52**, 3630–3636.
27 Q. Shen, I. Batashev, F. Zhang, H. Ojiyed, I. Dugulan, N. van Dijk and E. Brück, *Acta Mater.*, 2023, **257**, 119149.
28 L. Li, P. Tong, W. Tong, W. Jiang, Y. Ding, H. Lin, J. Lin, C. Yang, F. Zhu, X. Zhang, X. Zhu, W. Song and Y. Sun, *Inorg. Chem.*, 2019, **58**, 16818–16822.
29 Z. Tang, X. Wang, J. Li, C. He, C. Tang, H. Wang, M. Chen and T. Ouyang, *Appl. Phys. Lett.*, 2023, **122**, 172203.
30 Z. Tang, X. Wang, C. He, J. Li, M. Chen, C. Tang and T. Ouyang, *Phys. Rev. B*, 2024, **110**, 134320.
31 Q. Shen, Z. Zhang, C. de Vries, A. I. Dugulan, N. van Dijk, E. Brück and L. Li, *Chem. Mater.*, 2024, **36**, 6299–6305.
32 H. Wang, Y.-H. Wang, Y.-Y. Gong, G.-Z. Xu, E. Liu, X.-F. Miao, Y.-J. Zhang, Y.-Y. Shao, J. Liu and N. UI Hassan, *et al.*, *Rare Met.*, 2024, 1–10.
33 M. Xu, Y. Song, Y. Xu, Q. Sun, F. Long, N. Shi, Y. Qiao, C. Zhou, Y. Ren and J. Chen, *Chem. Mater.*, 2022, **34**, 9437–9445.
34 E. Wassermann, M. Acet, B. Rellinghaus and W. Pepperhoff, *J. Magn. Magn. Mater.*, 1995, **140–144**, 241–242.
35 E. F. Wassermann, B. Rellinghaus, T. Roessel, J. Kästner and W. Pepperhoff, *Eur. Phys. J. B*, 1998, **5**, 361–365.
36 E. Wassermann, B. Rellinghaus, T. Roessel and W. Pepperhoff, *J. Magn. Magn. Mater.*, 1998, **190**, 289–301.
37 G. Wertheim, J. Wernick and R. Sherwood, *Solid State Commun.*, 1969, **7**, 1399–1402.
38 P. J. Brown, J. Deportes and B. Ouladdiaf, *J. Phys.: Condens. Matter*, 1992, **4**, 10015.
39 Y. Song, M. Xu, X. Zheng, C. Zhou, N. Shi, Q. Huang, S. Wang, Y. Jiang, X. Xing and J. Chen, *J. Mater. Sci. Technol.*, 2023, **147**, 102–111.
40 Y. Song, Q. Sun, M. Xu, J. Zhang, Y. Hao, Y. Qiao, S. Zhang, Q. Huang, X. Xing and J. Chen, *Mater. Horiz.*, 2020, **7**, 275–281.
41 Y. Xinlin, C. Xing-Qiu, A. Grytsiv, P. Rogl, R. Podloucky, V. Witusiewicz, V. Pomjakushin and G. Giester, *Int. J. Mater. Res.*, 2022, **97**, 450–460.
42 L. Sun, H. Yibole, O. Tegus and F. Guillou, *Crystals*, 2020, **10**, 410.
43 L. van Eijck, L. D. Cussen, G. J. Sykora, E. M. Schooneveld, N. J. Rhodes, A. A. van Well and C. Pappas, *J. Appl. Crystallogr.*, 2016, **49**, 1398–1401.
44 V. Petříček, M. Dušek and L. Palatinus, *Z. Kristallogr. – Cryst. Mater.*, 2014, **229**, 345–352.
45 E. Welter, R. Chernikov, M. Herrmann and R. Nemausat, *AIP Conf. Proc.*, 2019, **2054**, 040002.
46 B. Ravel and M. Newville, *J. Synchrotron Radiat.*, 2005, **12**, 537.
47 W. Brückner, R. Perthel, K. Kleinstück and G. E. R. Schulze, *Phys. Status Solidi B*, 1968, **29**, 211–216.
48 L. Diop, O. Prokhnenko, O. Isnard, G. Ballon and J. Itié, *Intermetallics*, 2021, **129**, 107054.
49 N. Assoudi, M. Smari, I. Walha, E. Dhahri, S. Shevyrtalov, O. Dikaya and V. Rodionova, *Chem. Phys. Lett.*, 2018, **706**, 182–188.
50 B. Banerjee, *Phys. Lett.*, 1964, **12**, 16–17.
51 J. Köble and M. Huth, *Phys. Rev. B:Condens. Matter Mater. Phys.*, 2002, **66**, 144414.
52 J. Rehr, J. Kas, M. Prange, A. Sorini, Y. Takimoto and F. Vila, *C. R. Phys.*, 2009, **10**, 548–559.
53 E. Wassermann, *Phys. Scr.*, 1989, **1989**, 209.
54 P. Entel, E. Hoffmann, P. Mohn, K. Schwarz and V. Moruzzi, *Phys. Rev. B:Condens. Matter Mater. Phys.*, 1993, **47**, 8706.

